Numerical analysis of electron-wave detection by a wedge-shaped point contact

T. Usuki,* M. Takatsu, R. A. Kiehl, and N. Yokoyama
Quantum Electron Devices Laboratory, Fujitsu Laboratories Ltd., 10-1 Morinosato-Wakamiya, Atsugi 243-01, Japan
(Received 4 February 1994; revised manuscript received 29 April 1994)

To investigate useful properties caused by various interference effects of electron waves in a mesoscopic system, we carry out a numerical analysis of electron-wave propagation by a combination of several techniques for solving the two-dimensional Schrödinger equation. The techniques provide an accurate solution for a realistic potential profile in a point-contact structure, and are simple to apply even under magnetic fields. By using this calculation method, we investigate the detection of the propagation from a quantum point-contact injector to a point-contact detector under magnetic fields. We calculate electron-wave propagation and transfer conductance through a wedge-shaped detector, which has a smaller scattering cross section for injected electron waves than ordinary line-shaped detectors, and analyze the interference due to the detector as a function of detector parameters. We conclude that a well-designed wedge-shaped point contact could provide good detection of electron-wave propagation.

I. INTRODUCTION

Mesoscopic systems are interesting from the viewpoint of electronic transport. Mesoscopic phenomena have been measured in artificial systems with a variable confining potential. Recently, many studies have focused on the ballistic and wavelike behavior of electrons, using submicrometer lithographic techniques and high-mobility two-dimensional (2D) electron-gas structures, where the system dimensions are significantly smaller than the mean free path and the coherence length at low temperatures. Striking effects in such systems, including conductance quantization[1,2] and magnetic focusing,[3] have been measured on point contacts usually made from split Schottky-gate structures. Some of us have measured the transfer conductance across a series of two point contacts with varying magnetic field and observed the dependence of the characteristic on the mode number of the injector contact.[4] There are also many other experiments with point contacts in series.[5-11] In particular, the interference of electron waves has been used to investigate electron-electron scattering in 2D electron gases,[12] and the control of electron waves by an electrostatic potential has been investigated for possible device applications.[13-15]

Many theoretical studies have been done on mesoscopic phenomena. Many of the observed phenomena have been explained by the propagation of wave functions. Conductance quantization in a point contact, for example, can be explained in the adiabatic case.[16] In the nonadiabatic case, the conductance has been calculated for a quantum wire with an infinite confinement potential (hard wall) abruptly connected to the wide region, and this result clearly shows that the conductance strongly depends on the shape of the system.[17-20] In another case, a relatively complex shape dependence has been reported for the transfer conductance of a cross-shaped junction, and it has been pointed out that the reflected wave in this structure plays an important role in the electron transport.[21] There are also many other numerical analyses for crossed-wire structures, which show complicated properties of the conductance.[22-25] Additionally, it was found numerically that the conductance has random quantum properties when the confinement potential has a stadium-like shape.[26]

Although it has been made clear that the electronic transport in the ballistic region has various shape-dependent features, the transport calculations, to date, have been for almost ideally shaped structures, since it is difficult to calculate wave functions in 2D systems with a general shape, especially under magnetic fields. The structure of actual electron wave devices, however, has a complex shape which is neither completely adiabatic nor perfectly abrupt. To observe and control the useful properties of the transport, it is necessary to design the device structure so as to clearly separate desired property from undesired interference of electron waves, including the universal conductance fluctuations of mesoscopic systems. Thus we must find how to enhance the desired property in an optimized structure where undesired interference is suppressed.

In regard to investigating the desired properties, it is important to develop a general method of calculating conductance, which applies to realistic structures. There are some calculation methods suited for this situation. The recursive calculation of the Green function within the framework of a lattice model is one candidate.[21] The coupled-channel method[27] is also useful for such scattering problems. This method has the advantage of applicability to various potential profiles for the wire, and therefore we will use it here. However, this technique must be extended to more general geometries. In order to apply it to more general situations, its numerical stability must be improved. Furthermore, it is important to simplify the treatment of magnetic fields.

In this paper, we present a numerical study of electron-wave detection by a wedge-shaped point contact. We describe our calculation method for the conductance by solving the Schrödinger equation directly and analyze mesoscopic phenomena for a line-shaped point-contact

0163-1829/94/50(11)/7615(11)/$06.00

injector and a wedge-shaped point-contact detector. Details of the calculation method used to obtain the wave functions are given in Sec. II. This method is successful due to three essential ingredients: the transformation of a 2D system with a point contact into a quasi-1D system by using conformal mapping, the calculation of wave functions by the coupled-channel method with the choice of a suitable gauge, and an iteration technique which completely suppresses the numerical instability. In Sec. III, we apply this method to our geometry with a realistic potential profile. In Sec. IV, numerical results on magnetic steering and detection of electron waves are described. The effect of the interference due to a wedge-shaped detector on the conductance is examined through the calculation of transfer conductance from the injector to the detector. Finally, a summary is given in Sec. V.

II. CONDUCTANCE CALCULATION IN A TWO-DIMENSIONAL SYSTEM

The transport phenomena in mesoscopic systems can be investigated using the Landauer formula.[28,29] To obtain the conductance, then, we used a numerical calculation method for easily solving the time-independent 2D Schrödinger equation in the effective-mass approximation, where a magnetic field can be included in the calculation.

A. Transformation for the Hamiltonian

The coordinates as shown in Fig. 1, which we study here, are useful for calculations on a point contact. The 2D system consists of two outer regions of half an infinite plane and a finite region Γ. Γ has large enough dimensions to include various structures within the point contact. We consider the following Hamiltonian which describes the 2D system under a magnetic field $\mathbf{B}=(0,0,B_z)$ in the Γ region:

$$H=\frac{1}{2m^*}\left[\left[-i\hbar\frac{\partial}{\partial x}+eA_x\right]^2+\left[-i\hbar\frac{\partial}{\partial y}+eA_y\right]^2\right]+V(x,y)-E_F\ , \tag{2.1}$$

where m^* is the effective mass, the vector potential $\mathbf{A}=(A_x,A_y,0)$ satisfies $\mathbf{B}=\mathrm{rot}\,\mathbf{A}$, and V and E_F are the potential and Fermi energy, respectively.

In the Γ region, elliptic coordinates are used with the center at the point contact,[16,30] i.e., conformal mapping is done as

$$x=c\cosh u\cos v\ ,\qquad y=c\sinh u\sin v\ . \tag{2.2}$$

By means of the mapping, we transform the 2D electron system in the Γ region into a quasi-1D system, and the coupled-channel method is applied to the calculation only for wire structures.[27] For the following calculation, we choose the gauge as $A_u=0$. The transformed pseudo-Hamiltonian is given by

$$\tilde{H}=-\frac{\partial^2}{\partial u^2}-\left[\frac{\partial}{\partial v}+i\tilde{A}_v\right]^2+\tilde{V}(u,v)\ , \tag{2.3}$$

with

$$\tilde{A}_v=\frac{e}{\hbar}D^{1/2}A_v\ \text{ and }\ \tilde{V}=\frac{2m^*}{\hbar^2}D(V-E_F)\ , \tag{2.4}$$

where D is Jacobian, $c^2(\sinh^2 u+\sin^2 v)$. It is assumed that $V(x,0)=\infty$ for $|x|\geq c$; in particular, the potential V diverges faster than $1/D$ at $x=\pm c, y=0$. Then $\tilde{V}$ is infinite at this point, and the confining potential is almost along the v axis. We take $c=3\lambda_F$ in actual numerical calculations, where λ_F is the Fermi wavelength. This assumption is not inconsistent with actual systems.

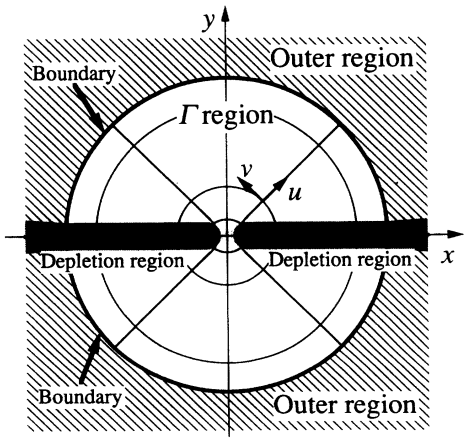

FIG. 1. Schematic drawing of elliptic coordinates for calculation in a point-contact structure. Shaded regions indicate depletion regions due to the point-contact structure. The 2D system is divided into two outer regions of half an infinite plane and a finite region Γ by two half-circle boundaries. The boundary condition is based on the continuity conditions for wave functions of plane waves and Hankel functions, and their gradients [see Eqs. (2.22)–(2.25)].

B. Calculation for the wave functions

The wave function $\Psi(u,v)$ for the transformed quasi-1D system in the Γ region satisfies the equation $\tilde{H}\Psi(u,v)=0$. This wave function is determined by the coupled-channel method. This method can be applied to various potential profiles within the framework of the quasi-1D system, and is precise for the conservation of flow. The Γ region is divided into a sufficiently large number N of small sections (see Fig. 2), and the u dependence of the potential is neglected in each section. The variables of the equation can then be separated for each function as follows:

$$\Psi_j^{(j)}(u,v)=\sum_{n=1}\chi_{jn}(u)\psi_{jn}^{(j)}(v)\ \text{ for } u_j\leq u\leq u_{j+1}\ , \tag{2.5}$$

where u_j is the boundary between the $(j-1)$th section and the jth section, for $1\leq j\leq N$. Here, the gauge of the jth section, which is indicated by the superscript (j) in Eq. (2.5), is chosen as

$$\tilde{A}_v^{(j)}=\frac{e}{\hbar}\int_{u_j}^{u}DB_z\,du\ , \tag{2.6}$$

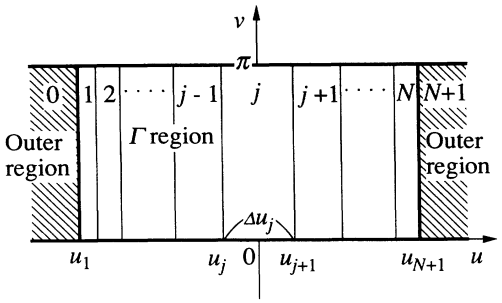

FIG. 2. Quasi-1D system transformed by conformal mapping. The Γ region is divided into a sufficiently large number N of small sections, and the u dependence of the effective potentials including the effective vector potential is neglected in each section.

where $\tilde{A}_{vj}^{(j)}(u_j)=0$. Furthermore, the u dependence of $\tilde{A}_v^{(j)}$ and $\tilde{V}$ is neglected in each section, and the approximate pseudopotentials in the jth section are given by

$$\tilde{A}_{vj}^{(i)}(v)=\tfrac{1}{2}[\tilde{A}_v^{(i)}(u_j,v)+\tilde{A}_v^{(i)}(u_{j+1},v)] , \tag{2.7}$$

and

$$\tilde{V}_j(v)=\tfrac{1}{2}[\tilde{V}(u_j,v)+\tilde{V}(u_{j+1},v)] . \tag{2.8}$$

Then, $\psi_{jn}^{(j)}(v)$ must satisfy the equations.

$$\left[\left[-i\frac{d}{dv}+\tilde{A}_{vj}^{(j)}(v)\right]^2+\tilde{V}_j(v)\right]\psi_{jn}^{(j)}(v)=\varepsilon_{jn}\psi_{jn}^{(j)}(v) , \tag{2.9}$$

where $\tilde{A}_{vj}^{(j+1)}=-\tilde{A}_{vj}^{(j)}$. The values ε_{jn} are determined from the above equation, and are equivalent to the values $-(h_m)^2$ of Eq. (10) in Ref. 30. The expression for the case of a uniform magnetic field is

$$\tilde{A}_{vj}^{(j)}(v)=\frac{ec^2}{8\hbar}B_z(\sinh 2u_{j+1}-\sinh 2u_j-2\Delta u_j\cos 2v)$$
$$\text{with } \Delta u_j=u_{j+1}-u_j . \tag{2.10}$$

Since the u dependence of the pseudopotentials is neglected, $\chi_{jn}(u)$ in Eq. (2.5) is a plane wave and is represented by

$$\chi_{jn}(u)=a_{jn}^{(+)}\exp(ik_{jn}u)+a_{jn}^{(-)}\exp(-ik_{jn}u)$$
$$\text{with } k_{jn}=\sqrt{-\varepsilon_{jn}} . \tag{2.11}$$

We also take into account the case where k_{jn} is imaginary ($\mathrm{Im}k_{jn}>0$).

The assumption of a steplike structure for the vector potential is useful, but it leads to infinite and quasiperiodic magnetic fields. Therefore it is possible that this assumption may result in complex interference of the wave function due to the quasiperiodicity. We take care to avoid such effects in our actual numerical calculations by our consideration of transmission matrices and spatial distributions of wave functions. We adopt the following limits as the numerical conditions. For the step length Δu_j, we require $\Delta u_j<h/(\pi ec^2B_z\cosh 2u_j)$ and $\Delta u_j<\lambda_F/(c\cosh u_j)$. These inequalities mean that the step length is smaller than the pseudo-cyclotron-radius and the pseudo-Fermi-wavelength in the transformed u-v space. Then, in the case of a Γ region with radius of $40\lambda_F$, the number of divisions N for the u axis must be in the range of 200–300. Furthermore, we investigate electronic properties only for $|B_z|<0.04h/(e\lambda_F^2)$, that is, in relatively weak fields. The transmission matrices and spatial distributions of wave functions were found to be insensitive to the step length, that is, these values sufficiently converged while within the above limitations.

The function of v can be expanded by the common basis $\phi_m(v)$ in all sections as

$$\psi_{jn}^{(j)}(v)\cong\sum_{m=1}^{M}f_{jmn}^{(j)}\phi_m(v) . \tag{2.12}$$

The basis function is satisfied by the boundary condition $\phi_m(0)=\phi_m(\pi)=0$. This method is characteristic of the coupled-channel method. When the basis set is sufficiently large, $M\simeq 150$ in this calculation, the function of v can be found for various confining potentials discussed here. For example, we could choose a sine function for the mth basis function, given by $\phi(v)=\sqrt{2/\pi}\sin(mv)$, which is useful when the system has relatively weak asymmetry on the v axis. In another case, the v axis is divided into widths Δv, and the basis function can be determined by

$$\phi_m(v)=\begin{cases}\dfrac{1}{\sqrt{\Delta v}} & \text{for } |v-v_m|<\dfrac{\Delta v}{2} ,\\ 0 & \text{for } |v-v_m|<\dfrac{\Delta v}{2} .\end{cases} \tag{2.13}$$

This discrete expression further simplifies the eigenvalue problem of Eq. (2.9). Accordingly, we will use this expression in the following formulation. Equation (2.9) is transformed into the eigenvalue problem represented by the coefficient $f_{jmn}^{(j)}$ in Eq. (2.12). Actually, to obtain $f_{jmn}^{(j)}$, we calculate an eigenvalue problem for the following matrix of real numbers:

$$\begin{bmatrix}h_{11} & h_{12} & 0 & \cdots & 0\\ h_{12} & h_{22} & h_{23} & & 0\\ 0 & h_{23} & h_{33} & & 0\\ \vdots & & & & \vdots\\ 0 & 0 & 0 & \cdots & h_{MM}\end{bmatrix}\begin{bmatrix}g_{1n}\\ g_{2n}\\ g_{3n}\\ \vdots\\ g_{Mn}\end{bmatrix}=-\varepsilon_{jn}\begin{bmatrix}g_{1n}\\ g_{2n}\\ g_{3n}\\ \vdots\\ g_{Mn}\end{bmatrix} , \tag{2.14}$$

with

$$h_{mm}=2\Delta v^{-2}+\frac{1}{2}\left[\tilde{V}_j\left[v_m-\frac{\Delta v}{2}\right]+\tilde{V}_j\left[v_m+\frac{\Delta v}{2}\right]\right] \tag{2.15}$$

and

$$h_{mm+1}=-\Delta v^{-2} .$$

Furthermore, we consider the factor for gauge transformation to be

$$U_m=\exp\left[-i\Delta v\left[\tfrac{1}{2}\tilde{A}^{(j)}_{jv}(v_m)+\sum_{l=1}^{m-1}\tilde{A}^{(j)}_{jv}(v_l)\right]\right]. \quad (2.16)$$

Then the coefficient $f^{(j)}_{jmn}$ is given by

$$f^{(j)}_{jmn}=U_m g_{mn} . \quad (2.17)$$

Note that as long as we use the discrete expression as a basis, the gauge transformation of the wave function from (j) to $(j+1)$ becomes the simple expression

$$f^{(j+1)}_{jmn}=f^{(j)*}_{jmn} , \quad (2.18)$$

where the asterisk means the complex conjugate. When another function is used as a basis, we have to choose the phase of each eigenvector to satisfy this relation.

By using continuity conditions for the wave function and its gradient, we can connect the wave function of a section to those of adjacent sections as follows:

$$\begin{bmatrix}\mathbf{a}^{(+)}_{j+1}\\ \mathbf{a}^{(-)}_{j+1}\end{bmatrix}=\mathbf{S}_j\begin{bmatrix}\mathbf{a}^{(+)}_{j}\\ \mathbf{a}^{(-)}_{j}\end{bmatrix}, \quad (2.19)$$

where $\mathbf{a}^{(\pm)}_j={}^T(a^{(\pm)}_j M)$, and the $2M\times 2M$ matrix $\mathbf{S}_j$ is given by

$$\mathbf{S}_j=\begin{bmatrix}\mathbf{s}_j(+,+) & \mathbf{s}_j(+,-)\\ \mathbf{s}_j(-,+) & \mathbf{s}_j(-,-)\end{bmatrix}, \quad (2.20)$$

and

$$s_{jmn}(\sigma,\sigma')=\frac{1}{2}\left[1+\sigma\sigma'\frac{k_{jn}}{k_{j+1\,m}}\right]\exp(i\sigma' k_{jn}\Delta u_j)\times\sum_{l=1} f^{(j+1)*}_{j+1\,lm}f^{(j+1)}_{jln} \quad \text{as } \sigma,\sigma'=\pm 1 . \quad (2.21)$$

The wave function in Γ is obtained by iterating Eq. (2.19) from the first section to the Nth section. In contrast to mode matching, which is only applicable to simple potential profiles, the wave function in the coupled-channel method satisfies the conservation of flow correctly because of the orthogonality of the basis. Even under a magnetic field $\mathbf{B}$ perpendicular to a 2D system, the 2D Schrödinger equation is solved by nearly the same method as it would be without a magnetic field, by using the optimized vector potential in each section. To calculate the conductance for a point contact, we have to obtain the wave function in the open system including Γ and the two outer regions. Thus it is necessary that the wave function obtained in Γ is connected to the wave functions of the outer regions by polar coordinates on boundaries (see Fig. 1). Here, the ingoing (outgoing) outer region is named section $0(N+1)$, as indicated in Fig. 2. For example, we could apply the mode-matching method to the connection.[20] However, the coupled-channel method is also applied to connecting the two outer regions with Γ, when the Γ region is sufficiently large. In this case, i.e., $\exp|u_0|,\exp|u_{N+1}| \gg c/\lambda_F$, elliptic coordinates near the boundaries are nearly polar coordinates. In the outer regions, we assume that the potential V is proportion to $\exp(-|u|)$ and the magnetic field is zero, i.e., $\tilde{A}^{(0)}_{v0}=0$ and $\tilde{A}^{(N+1)}_{v\,N+1}=0$. Then the wave function changes adiabatically in these regions. Under these conditions the function $\psi^{(j)}_{jn}(v)$ is given by

$$\left[-\frac{d^2}{dv^2}+\tilde{V}_j(v)\right]\psi^{(j)}_{jn}(v)=\varepsilon_{jn}\psi^{(j)}_{jn}(v) \quad \text{as } j=0,N+1 . \quad (2.22)$$

Here, the potentials are defined as

$$\tilde{V}_0(v)=\frac{c^2 m^*}{2\hbar^2}e^{-2u_1}V(u_1,v) ,$$

and

$$\tilde{V}_{N+1}(v)=\frac{c^2 m^*}{2\hbar^2}e^{2u_{N+1}}V(u_{N+1},v) . \quad (2.23)$$

We use a Hankel function of the first kind $H^{(1)}_\nu$ for the u axis instead of a plane wave, and the expression for connecting the outer region with Γ is modified from Eq. (2.21). The connection from the 0th section to the first section is given by

$$s_{0mn}(\sigma,\sigma')=\frac{1}{2}\left[\chi^{(\sigma')}_{0n}+\sigma\frac{\chi^{(\sigma')'}_{0n}}{ik_1}\right]\sum_{l=1} f^{(1)*}_{1lm}f^{(1)}_{0ln} , \quad (2.24)$$

where $\chi^{(-)}_{0n}=H^{(1)}_\nu(2\pi c e^{-u_1}/\lambda_F)$

$$\chi^{(-)'}_{0n}=[dH^{(1)}_\nu(2\pi c e^{-u}/\lambda_F)/du]_{u=u_1} ,$$

and $\chi^{(+)}_{0n}=\chi^{(-)*}_{0n}$ with $\nu=\sqrt{\varepsilon_{0n}}$. Furthermore, the connection from the Nth section to the $(N+1)$th section is given by

$$s_{Nmn}(\sigma,\sigma')=\frac{\sigma(\chi^{(-\sigma)'}_{N+1m}-i\sigma' k_{Nn}\chi^{(-\sigma)}_{N+1\,m})}{\chi^{(+)}_{N+1\,m}\chi^{(-)'}_{N+1\,m}-\chi^{(+)'}_{N+1\,m}\chi^{(-)}_{N+1\,m}}\times\exp(i\sigma' k_{Nn}\Delta u_N)\sum_{l=1} f^{(N+1)*}_{N+1\,lm}f^{(N+1)}_{Nln} , \quad (2.25)$$

where

$$\chi^{(+)}_{N+1\,n}=H^{(1)}_\nu(2\pi c e^{u_{N+1}}/\lambda_F) ,$$

$$\chi^{(+)'}_{N+1\,n}=[dH^{(1)}_\nu(2\pi c e^{u}/\lambda_F)/du]_{u=u_{N+1}} ,$$

and $\chi^{(-)}_{N+1\,n}=\chi^{(+)*}_{N+1\,n}$ with $\nu=\sqrt{\varepsilon_{N+1\,n}}$. These expression can be applied to connect the wave functions to the outer regions.

C. Iteration technique for the conductance calculation

From these equations, the whole wave function from one outer region to another is simply obtained by the coupled-channel method, and therefore we can obtain the transmission probability $|T_{mn}|^2$ from the incident channel n the outgoing channel m. In terms of the transmission probability, the conductance G of the system is obtained by the multichannel version of the Landauer formula,[31]

$$G=\frac{2e^2}{h}\sum_{m,n}|T_{mn}|^2 . \quad (2.26)$$

The matrix $\mathbf{T}$ of the transmission wave is defined by

$$\begin{bmatrix} \mathbf{T} \\ \mathbf{0} \end{bmatrix} = \mathbf{S}_N \mathbf{S}_{N-1} \cdots \mathbf{S}_0 \begin{bmatrix} \mathbf{1} \\ \mathbf{R} \end{bmatrix} . \tag{2.27}$$

Note, however, that numerical calculation for the above equation is extremely unstable in general. To suppress the instability, we actually use the following iteration technique:

$$\begin{bmatrix} \mathbf{t}_R^{(j+1)} & \mathbf{r}_R^{(j+1)} \\ \mathbf{0} & \mathbf{1} \end{bmatrix} = \mathbf{S}_j \begin{bmatrix} \mathbf{t}_R^{(j)} & \mathbf{r}_R^{(j)} \\ \mathbf{0} & \mathbf{1} \end{bmatrix} \mathbf{P}_j , \tag{2.28}$$

with

$$\mathbf{P}_j = \begin{bmatrix} \mathbf{1} & \mathbf{0} \\ \mathbf{p}_{j1} & \mathbf{p}_{j2} \end{bmatrix} . \tag{2.29}$$

Here the initial condition of the iteration is $\mathbf{t}_R^{(0)}=\mathbf{1}$, $\mathbf{r}_R^{(0)}=\mathbf{0}$, and the matrix $\mathbf{P}_j$ is a linear operator to satisfy the form which is assigned to the matrix at the left side of Eq. (2.28). Then we treat this linear operator for each connecting step in the computation. The detailed expressions are given by

$$\mathbf{p}_{j1} = -\mathbf{p}_{j2} \mathbf{s}_j(-,+) \mathbf{t}_R^{(j)} , \tag{2.30}$$

and

$$\mathbf{p}_{j2} = [\mathbf{s}_{j(-,+)} \mathbf{r}_R^{(j)} + \mathbf{s}_{j(-,-)}]^{-1} . \tag{2.31}$$

This iteration continues from $J=0$ to N, and it finally gives $\mathbf{T}=\mathbf{t}_R^{(N+1)}$. Additionally, a similar iteration gives the matrix $\mathbf{R}$ of the reflection wave as

$$\begin{bmatrix} \mathbf{1} & \mathbf{0} \\ \mathbf{r}_L^{(i+1)} & \mathbf{t}_L^{(j+1)} \end{bmatrix} = \begin{bmatrix} \mathbf{1} & \mathbf{0} \\ \mathbf{r}_L^{(j)} & \mathbf{t}_L^{(j)} \end{bmatrix} \mathbf{P}_j , \tag{2.32}$$

and

$$\mathbf{R} = \mathbf{r}_L^{(N+1)} ,$$

where the initial condition is $\mathbf{t}_L^{(0)}=\mathbf{1}, \mathbf{r}_L^{(0)}=\mathbf{0}$. In order to obtain the electron density at an arbitrary point, we define a row vector and calculate iteratively as follows:

$$(\phi_1^{(i,i)}, \ldots, \phi_{2M}^{(i,i)}) \equiv (\psi_{i1}^{(i)}(v), \ldots, \psi_{iM}^{(i)}(v), \psi_{i1}^{(i)}(v), \ldots, \psi_{iM}^{(i)}(v)) \times \begin{bmatrix} \mathbf{t}_R^{(i)} & \mathbf{r}_R^{(i)} \\ \mathbf{0} & \mathbf{1} \end{bmatrix} , \tag{2.33}$$

and

$$(\phi_1^{(j+1,i)}, \ldots, \phi_{2M}^{(j+1,i)}) = (\phi_1^{(j,i)}, \ldots, \phi_{2M}^{(j,i)}) \mathbf{P}_j \quad \text{for } i \le j \le N . \tag{2.34}$$

Then the electron density is obtained by

$$n(u_i, v) = \sum_{l=1}^{M} |\phi_l^{(N+1,i)}|^2 . \tag{2.35}$$

This iteration technique is useful for obtaining stable calculations, since its operation cancels divergence factors which occur due to numerical error in each step. Furthermore, it is applicable not only to the coupled-channel method but also to the lattice model,[32,33] where it can be used as an alternate method for connecting wave functions in the two regions (see Appendix). The advantage compared with the Green's function method in Ref. 21 is that the transfer matrix and electron wave at any point can be obtained at the same time by means of the linear operator $\mathbf{P}_j$.

To study the characteristics at finite temperature, our calculation method has to be extended. This application to finite temperature is easily possible with well-known techniques.[17,18] Interference is expected to be reduced at finite temperatures due to smearing. The numerical analysis below, however, is done only at zero temperature, since our main purpose is the investigation of the enhancement of useful electron-wave propagation properties and the suppression of unwanted interference.

III. A QUANTUM POINT CONTACT

To date, many calculations for point contacts have been done, but the structures have been very simplified. The propagation of a ballistic electron wave in realistic structures has not been investigated theoretically, although it is sensitive to the shape. In this section, we consider a point-contact structure with a realistic potential profile. In addition, preliminary calculations for the conductance and the angular distribution (collimation effect) of ballistic electron propagation are given for this structure. In the following, we measure almost all quantities in units relating to the 2D electron-gas parameters, i.e., energy is measured in units of the Fermi energy E_F and length in units of the Fermi wavelength λ_F. Furthermore, the magnetic field is measured in units of $h/(e\lambda_F^2)$. Then the magnetic field units are represented by the ratio of the Fermi wavelength and the classical cyclotron radius. The following numerical calculations have been performed on the Fujitsu VP-2400 Supercomputer.

A hard-wall potential is usually used in the numerical analysis of mesoscopic systems because the calculation of wave functions is simple for this potential. However, it has been reported that the confinement potential of the quantum wire caused by a split gate has a parabolic shape.[34] Therefore we assume that a point contact's lateral potential profile is composed of a parabola, and it has symmetry for the x and y axes. When $x,y>0$, a detailed potential profile is given by the expressions

$$V(x,y) = (R_1 + 1 - y)^2 \tag{3.1a}$$

when x,y are in region I indicated in Fig. 3(a),

$$V(x,y) = (R_1 + 1 - r)^2 \tag{3.1b}$$

when x,y are in region II, and

$$V(x,y) = 1 - \left[R_1 - \frac{W_1 + 2x}{W_1 - 2x} r \right] (R_1 - r) \tag{3.1c}$$

when x,y are in the region III. Here, $r=[(W_1/2-x)^2+y^2]^{1/2}$. In the other regions, $V(x,y)=0$. The potential of a point contact has only two parameters, R_1 and W_1. As shown in Fig. 3(a), R_1 is the half-circle radius of the potential and relates to the width of the depletion region in the 2D electron gas. We use $W_1=14$ in this paper. This value is suitable for a device having about a 0.2 μm gate length, 0.4 μm gate opening,

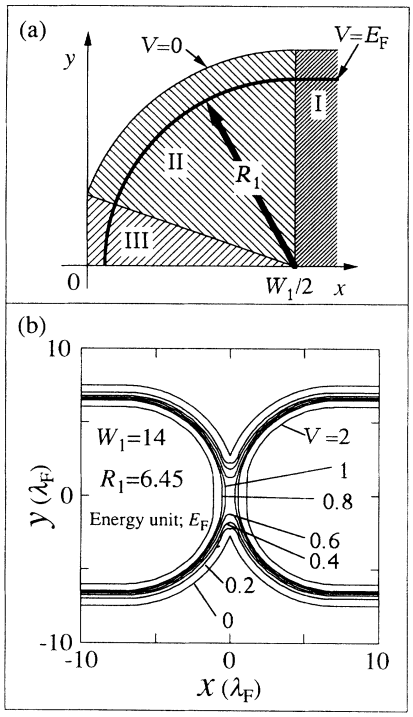

FIG. 3. (a) Schematic picture of Eqs. (3.1a)–(3.1c). Note that only the region of $x,y>0$ is shown. (b) Top view of a point-contact potential with $R_1=6.45$. Note that we did not draw higher potential lines than $V=2$, since these lines make the figure complex.

and 40 nm Fermi wavelength. These dimensions are reasonable for most mesoscopic experiments. For example, Fig. 3(b) shows the top view of a point-contact potential with $R_1=6.45$. The center of the point contact is a saddle point, and the potential profile along the x axis has a completely parabolic shape. We think that this potential is very similar to that in actual devices.

Figure 4 shows the conductance as a function of R_1 as calculated by our model. In the following, we use the specific values $R_1=6.45$ and 6.2, as typical cases for the first and second conductance plateaus, respectively. The figure shows a clearly quantized conductance. The change of the conductance does not have the complex structure due to resonance which occurs in the simpler abrupt point contact.[17–20]

The collimation effect is important for some experiments, for example, steering by magnetic fields,[5] and depends on the shape of the point-contact structure. The hard-wall potential has been used in calculations of collimation effects in point contacts.[35] In order to clearly illustrate the difference between the collimation effect in a realistic structure and in a simple structure, Fig. 5 shows two angular distributions of the injected electron at infinite distance from a point contact calculated from our model. One case is a realistic potential with $R_1=6.45$ as shown in Fig. 3(b). The other case is that of a point contact with both a square potential profile and an abrupt configuration (see inset in Fig. 5). The parameter values used in Fig. 5 were chosen to correspond to the center of the first plateau in both cases, and therefore provide a good comparison of the structures. The angular distributions in Fig. 5 and elsewhere in this paper are normalized such that their angular integral equals the conductance in units of $2e^2/h$. As evident from the results, the full width at half maximum of the angular distribution is one-half as wide for the realistic point contact as for the abrupt case. Thus the collimation significantly affects the propagation of electron waves in actual devices. Furthermore, examination of the results for other points within the plateau showed that the angular distribution hardly changes with R_1 within the limit of a plateau. This means that the angular distribution should be insensitive to small (<0.1 V) variations in bias voltage, in contrast to what might be expected from previous calculations.[36]

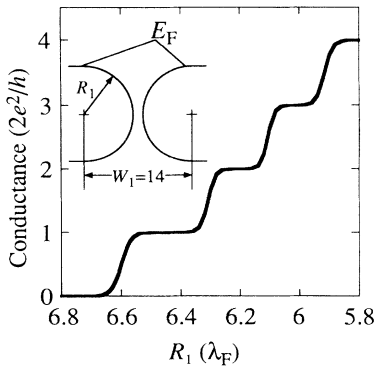

FIG. 4. Conductance of the point contact with changing R_1. The conductance of a realistic point-contact structure is clearly quantized.

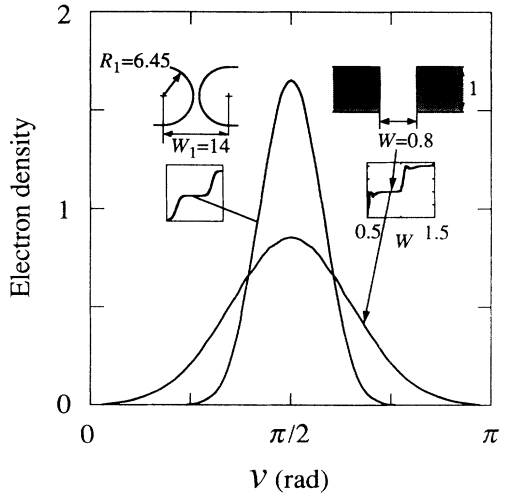

FIG. 5. Angular distribution of the injected electron at infinite distance from the point contact. A comparison of the collimation effect for a realistic and an abrupt configuration is given. Dimensions and conductance of the abrupt configuration are indicated in the inset. The electron density is normalized so that its angular integral is equal to the conductance (units of $2e^2/h$).

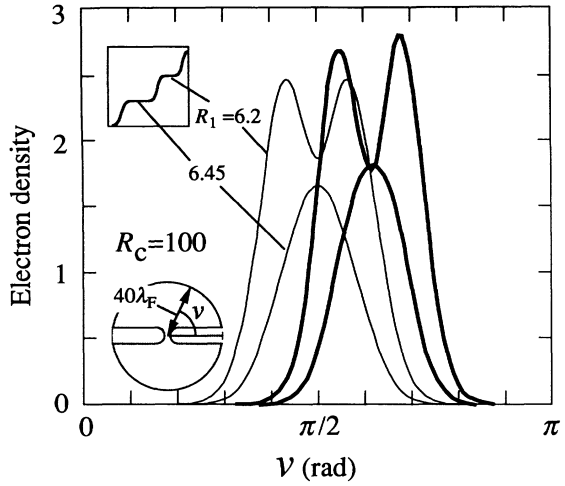

FIG. 6. Angular distribution under a magnetic field. Bold lines show the case for an applied magnetic field with $R_c = 100$ in a circle of radius 40. Narrow lines show the no-magnetic-field case. The distribution has a clearly single (double) peak structure in the case of $R_1 = 6.45(6.2)$, and the collimation also affects the propagation with the double peak.

IV. DETECTION OF ELECTRON WAVES

A. Steering by a magnetic field

Previous numerical studies obtained propagation under magnetic fields only for a simple structure composed of a wire and a half plane with hard walls.[37,38] The angular distribution has been studied in the weak-field approximation, and it was shown that the characteristic distribution at zero field is still conserved under the weak-field limit.[36] In this section, we investigate the magnetic-field dependence of the injected-electron propagation through a realistic point-contact structure. Figure 6 shows the angular distributions under a magnetic field with the cyclotron radius $R_c = 100$ in the cases of $R_1 = 6.45$ and 6.2. To apply our method, we must assume that the area with magnetic field is finite. Here this area consists of a circle with a radius of $40\lambda_F$ (~ 1.8 μm in an actual device) at the center of the point contact as indicated in the inset of Fig. 6. A previous calculation pointed out that reflection occurs at the boundary between regions with an applied magnetic field and no magnetic field.[39] Although we neglect this reflection in our cases, this does not seriously affect the following investigation, since the reflections of electron waves at the boundaries, which can hardly change the total conductance, are very weak.

It is clear from Fig. 6 that both the one-mode and two-mode cases are well collimated with a magnetic field. In the case of an applied magnetic field (shown by bold lines), the distributions shift from the center, and are slightly distorted by both the point-contact wall and the deviation due to the magnetic field. However, the distributions keep the characteristic peak structure at zero field. Figures 7(a) and 7(b) show the spatial distributions of injected electrons under a magnetic field with $R_c = 50$, when the angular distributions have single and double peaks, respectively. These electron waves propagate along classical orbits while keeping the symmetries of channels in the point contact, as indicated with bold arrows in the figures. As evident from the angular and spatial distributions, the propagation directly depends on the electron distribution within an actual point contact even under magnetic fields, thereby illustrating that the injected electron is useful for probing the quasi-1D channel states. However, these results are in the case of a point contact with no detector, and we have to investigate exactly the turbulence of electron-wave propagation by the detector.

B. Detection by a wedge-shaped point contact

We now calculate the propagation and the transfer conductance from an injector to a detector under magnetic fields. The configuration of the device, which consists of two point contacts, a line-shaped injector and a wedge-shaped detector, is shown as Fig. 8(a). The detector makes an angle with the injector so as to minimize its cross section. Furthermore, its orifice is wider than the injector, since the transfer conductance depends on the mode number of the detector as mentioned in Ref. 21. Here, the transfer conductance is determined by the scattering probability to the detector region, which is one of three regions, as shown in Fig. 8(b), and the eigenvalue problem for Eq. (2.14) is also divided into three parts. The basis-set number for the function of v has to be

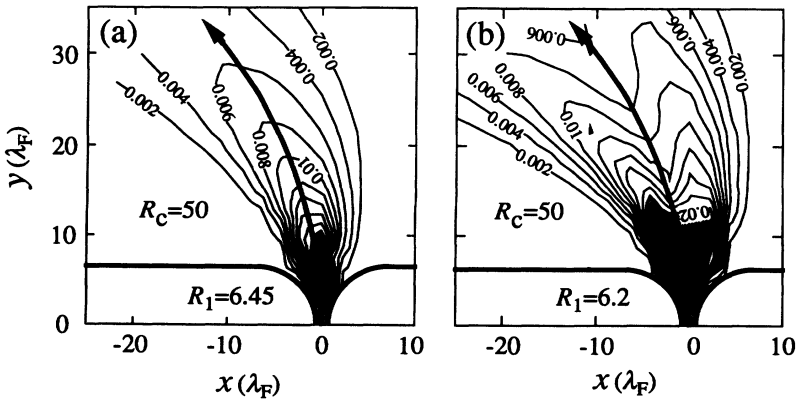

FIG. 7. Spatial distributions of the injected electrons under a magnetic field with $R_c = 50$. Bold arrows are classical cyclotron orbits. (a) $R_1 = 6.45$, (b) $R_1 = 6.2$. The shaded regions indicate an electron density greater than 0.02, since the contours would make the figure complex.

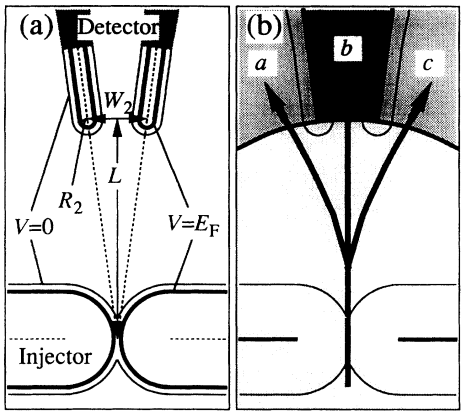

FIG. 8. Configuration of the device which consists of two point contacts as an injector and a detector. (a) Parameters of the detector are indicated. L is the distance between the detector's orifice and the injector. (b) Schematic picture illustrating the method of calculation of transfer conductance.

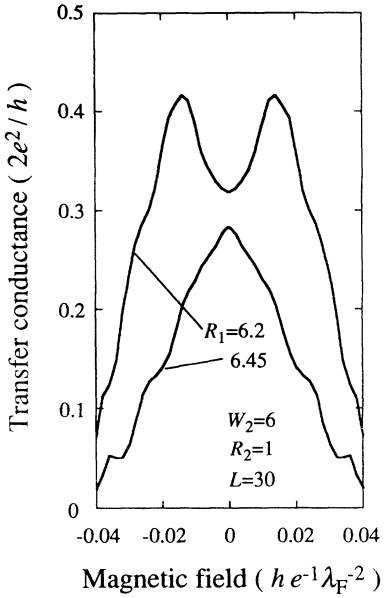

FIG. 10. Typical magnetic-field dependence of the transfer conductance in the cases that one mode and two modes exist in the injector with $R_1 = 6.45$, 6.2. Other parameters are the same as in Fig. 9.

sufficiently large in order to keep accuracy of transfer conductance. These numerical calculations require $M = 300$.

Figures 9(a) and 9(b) show typical spatial distributions for the structure under a magnetic field with $R_c = 50$ corresponding to the cases in Figs. 7(a) and 7(b), i.e., $R_1 = 6.45$ and 6.2. The detector in Fig. 9 has $W_2 = 6$ and $R_2 = 1$. The distance between the detector's orifice and the injector is $L = 30$. In comparison with the cases with no detector in Fig. 7, there is much scattering by the detector and complicated interference exists, especially near the detector's orifice. It may be inferred from the distributions that this scattering and interference may seriously affect the detection. However, the transfer conductance maintains the character of injected-electron propagation without a detector, as is evident from the numerical results in Fig. 10. This figure shows the magnetic-field dependence of the transfer conductance for the same devices as Fig. 9. The magnetic-field dependence with two (one) modes in the injector has a clear double (single) peak due to the symmetry of a second (first) electron-wave mode similar to Fig. 6, and small distortions by scatterings and interferences also occur in both the one- and two-mode cases.

To investigate the dependence of the transfer conductance on detector shape in detail, we focus on the double-peak structure for the two-mode case in the following. Figure 11 shows several plots with varying orifice parameter W_2. The detector's resolving power obviously becomes better with the narrowing of the orifice. In the narrowest case $W_2 = 4$, however, the detector has only three occupied modes at its orifice, and therefore the transfer conductance is more distorted than in the wider

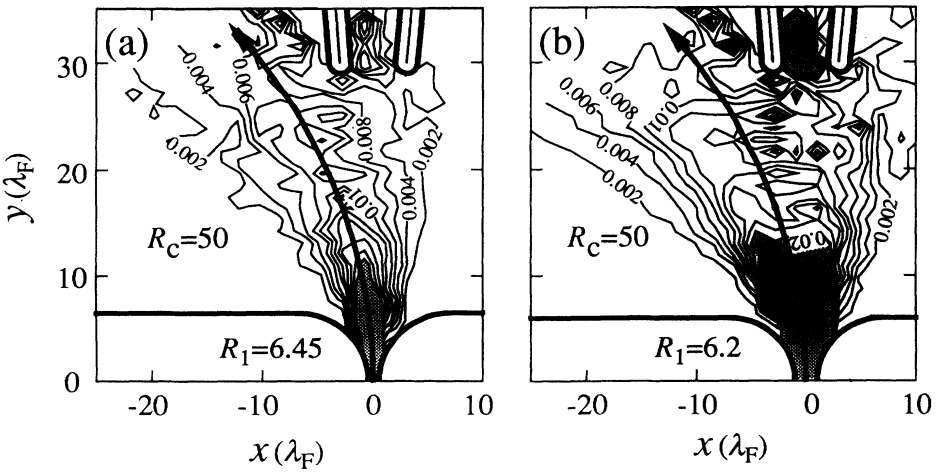

FIG. 9. Spatial distributions of the injected electron under a magnetic field with $R_c = 50$ with a wedge-shaped detector. (a) $R_1 = 6.45$, (b) $R_1 = 6.2$. The detector's parameters are $L = 30$, $R_2 = 1$, and $W_2 = 6$.

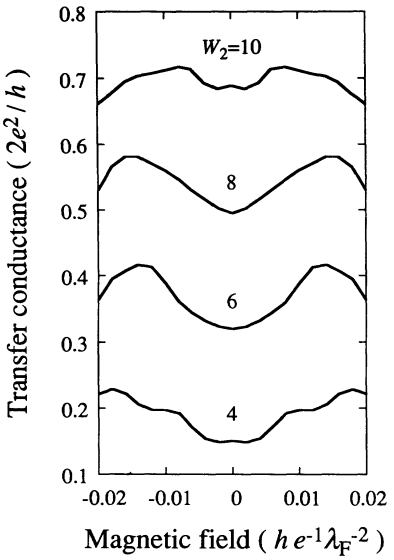

FIG. 11. Magnetic-field dependence of the transfer conductance as $R_1=6.2$ with varying orifice parameter W_2 of the detector.

cases. Figure 12(a) shows the transfer conductance with varying detector gate length R_2. With increasing length, the transfer conductance decreases, since the scattering cross section for electron-wave propagation increases. Furthermore, the distortion of the peak structure increases due to the scatterings and the interferences. In Figs. 12(b) and 12(c), we compare transfer conductances for two different values of L. The parameters are $L=30$, $W_2=8$, and $R_2=0,1,2$ in Fig. 12(b), and the device scale for these parameters in Fig. 12(c) is half that in Fig. 12(b). In spite of increasing multiple scattering between the injector and the detector, the results in Fig. 12(c) have similar values and characteristics as in Fig. 12(b). Note that the scale for the magnetic field in Fig. 12(c) is twice that of Fig. 12(b). Comparison of Figs. 12(b) and 12(c) shows that scaling approximately holds for the detector's simple parameters and the magnetic field even when the injector's parameters and detailed potential profile keep the same values. Consequently, present electron-beam lithography and a high-mobility 2D system are sufficient for realizing such devices as shown in Fig. 8(a) for detailed investigation of electron-wave properties in 2D electron gases. Furthermore, according to the above scaling rule, a finer structure for the detector is made unnecessary by increasing the distance L.

V. SUMMARY

We have described a calculation method for electron-wave propagation in 2D systems which can be applied to devices with any shape by means of both appropriate conformal mapping and the coupled-channel method. This method can be applied to an arbitrary potential and allows the wave functions to be simply obtained even under a magnetic field by choosing a suitable gauge. Furthermore, the iteration technique can realize stable numerical calculations and can maintain the conservation of flow; the most important condition for conductance calculation.

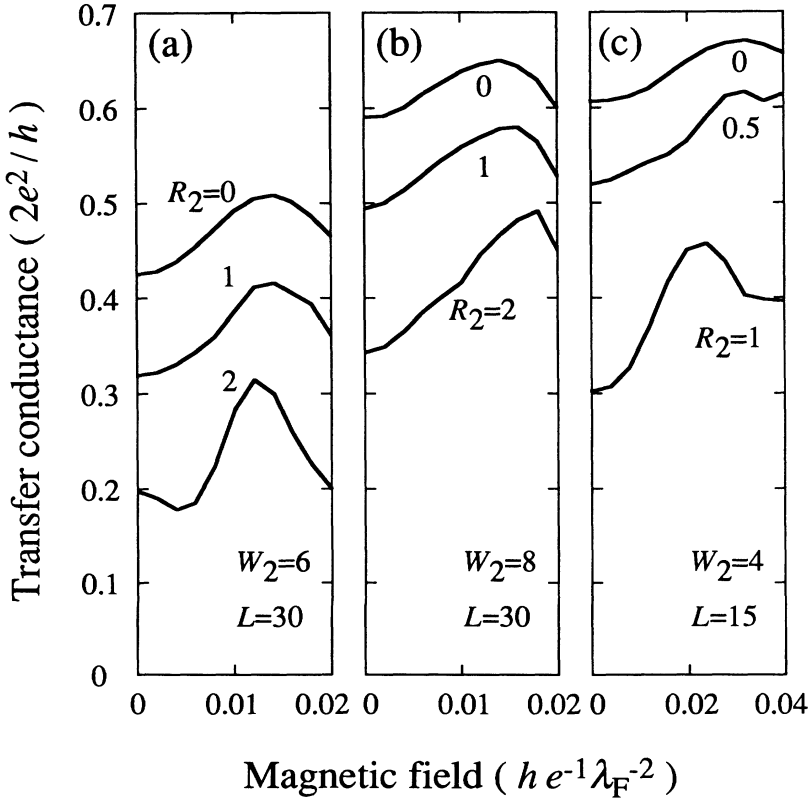

FIG. 12. Magnetic-field dependence of the transfer conductance at $R_1=6.2$ with varying R_2 and L. (a) $R_2=0.1,2$ with $W_2=6$ and $L=30$. (b) $R_2=0,1,2$ with $W_2=8$ and $L=30$. (c) $R_2=0,0.5,1$ with $W_2=4$ and $L=15$. Note that the scale for the magnetic field in (c) is twice that of (a) and (b).

Numerical results presented for several devices show that our simulation is useful for investigating the propagation in 2D systems and in designing mesoscopic devices. The point-contact injector examined in this paper corresponds to that used in many experiments. As evident from the angular distribution in Fig. 5, the roundness of the corners in an actual injector has a significant effect on the collimation of the electron-wave propagation. Results under a magnetic field in Figs. 6 and 7 confirm that the steering by magnetic fields does not disturb the modal nature of the propagation.

The numerical results for the transfer conductance, i.e., detection of a ballistic electron wave, are the most important in this paper, since point contacts in series are of interest for many basic and applied studies. Our results show that the transfer-conductance characteristic of a wedge-shaped detector with optimized spacing exhibits some distortion, but is clearly related to the symmetry of the injected waves. In particular, our results for two-mode injection $R_2=6.2$ show that good detector characteristics are obtained for $W_2<10$, which ensures a small enough orifice to resolve the spatial distribution, and for $W_2>4$, which ensures an adequate number of detector modes to represent the distribution. In addition, by using the scaling rule of the detector, good characteristics can be observed in a device with large dimension when a high-mobility sample is used.[40] The parameters $L=30$ and $W_2=6$ used in the calculations correspond to about 1.2 and 0.25 μm in actual devices. Hence, these results could be realized by using the present high-mobility 2D systems and electron-beam lithography.

The numerical results presented in this paper demonstrate the feasibility of studying ballistic electron-wave properties using optimized injector and detector geometries. By further developing the numerical analysis, for example, by coupling the present method with Poisson's equation to obtain a more realistic potential, we could more quantitatively predict electron-wave properties in mesoscopic devices.

ACKNOWLEDGMENTS

The authors express their sincere thanks to Professor T. Ando and Professor T. Ikoma in the University of Tokyo for their aid in the University Industry Joint Research "Mesoscopic Electrons." We also thank Professor A. Okiji, Professor H. Kasai, and K. Mitsutake in Osaka University for helpful discussion on the coupled-channel method. Especially, we thank Dr. S. Tarutya and Y. Tokura in NTT Basic Research Laboratories for useful comments on both physics and numerical calculation. Finally, we would like to thank M. Saito, M. Okada, and T. Futatsugi for showing us their experimental results and useful discussion.

APPENDIX

The following shows that the iteration technique based on Eqs. (2.28)–(2.32) is also applicable to a lattice model. The Hamiltonian of the lattice model is given by

$$\sum_j \mathbf{a}_j^\dagger(\mathbf{H}_j-E_F)\mathbf{a}_j+\mathbf{a}_j^\dagger\mathbf{H}_{j,j+1}\mathbf{a}_{j+1}+\mathbf{a}_j^\dagger\mathbf{H}_{j,j-1}\mathbf{a}_{j-1}\ ,$$

where $\mathbf{a}_j$ is a column vector which consists of annihilation operators in the jth column as $\mathbf{a}_j={}^T(a_{j,1},\ldots,a_{j,M})$. The states of the $2M$ channels (for right- and left-going electrons) in ideal wires, which include $j=1,2$ and $N-1,N$, respectively, are expressed by using two $M\times M$ matrices as

$$\mathbf{U}(\pm)=(\mathbf{u}_1(\pm),\ldots,\mathbf{u}_M(\pm))\ .$$

Thus the phase factors of the $2M$ channels from one column to the next in the wires are given by

$$\boldsymbol{\lambda}(\pm)=\mathrm{diag}[\lambda_1(\pm),\ldots,\lambda_M(\pm)]\ .$$

By using these expressions, the matrices of Eq. (2.20) are defined as

$$\mathbf{S}_0=\begin{bmatrix}\mathbf{U}(+) & \mathbf{U}(-)\\ \mathbf{U}(+)\boldsymbol{\lambda}(+) & \mathbf{U}(-)\boldsymbol{\lambda}(-)\end{bmatrix},$$

$$\mathbf{S}_j=\begin{bmatrix}\mathbf{0} & \mathbf{1}\\ -\mathbf{H}_{j,j+1}^{-1}\mathbf{H}_{j,j-1} & \mathbf{H}_{j,j+1}^{-1}(E_F-\mathbf{H}_j)\end{bmatrix}\quad \text{for } 1\le j\le N-1\ ,$$

and

$$\mathbf{S}_N=\mathbf{S}_0^{-1}\ .$$

By applying the $\mathbf{S}_j$ in the lattice model to the iteration of Eqs. (2.28)–(2.32), one can stably obtain a transmission matrix and electron density.

*FAX: +81-462-48-5193.

[1]B. J. van Wees, H. van Houten, C. W. J. Beenakker, J. G. Williamson, L. P. Kouwenhoven, D. van der Marel, and C. T. Foxon, Phys. Rev. Lett. **60**, 848 (1988).

[2]D. A. Wharam, T. J. Thornton, R. Newbury, M. Pepper, H. Ahmed, J. E. F. Frost, D. G. Hasko, D. C. Peacock, D. A. Ritchie, and G. A. C. Jones, J. Phys. C **21**, L209 (1988).

[3]H. van Houten, C. W. J. Beenakker, J. G. Williamson, M. E. I. Broekaart, P. H. M. van Loosdrecht, B. J. van Wees, J. E. Mooij, C. T. Foxon, and J. J. Harris, Phys. Rev. B **39**, 8556 (1989).

[4]M. Saito, M. Okada, M. Takatsu, and N. Yokoyama, Trans. IEE Jpn. **110-C**, 749, 1990 (in Japanese); M. Okada, M. Saito, M. Takatsu, K. Kosemura, T. Nagata, H. Ishiwari, and N. Yokoyama, Superlatt. Microstruct. **10**, 493 (1991); M. Okada, M. Saito, M. Takatsu, P. E. Schmidt, K. Kosemura, and N. Yokoyama, Semicond. Sci. Technol. **7**, B223 (1992).

[5]L. W. Molenkamp, A. A. M. Staring, C. W. J. Beenakker, R. Eppenga, C. E. Timmering, J. G. Williamson, C. J. P. M. Harmans, and C. T. Foxon, Phys. Rev. B **41**, 1274 (1990).

[6]T. Kakuta, Y. Takagaki, K. Gamo, S. Namba, S. Takaoka, and K. Murase, Phys. Rev. B **43**, 14 321 (1991).
[7]R. Behringer, G. Timp, H. U. Baranger, and J. E. Cunningham, Phys. Rev. Lett. **66**, 930 (1991).
[8]D. R. S. Cumming, H. Ahmed, and T. J. Thornton, Appl. Phys. Lett. **60**, 2755 (1992).
[9]S. Yamada, M. Yamamoto, and K. Aihara, Surf. Sci. **263**, 265 (1992).
[10]K. L. Shepard, M. L. Roukes, and B. P. Van der Gaag, Phys. Rev. Lett. **68**, 2660 (1992).
[11]T. Bever, Y. Hirayama, and T. Tarucha, J. Appl. Phys. **75**, 2477 (1994).
[12]A. Yacoby, U. Sivan, C. P. Umbach, and J. M. Hong, Phys. Rev. Lett. **66**, 1938 (1991).
[13]U. Sivan, M. Heiblum, C. P. Umbach, and H. Shtrikman, Phys. Rev. B **41**, 7937 (1990).
[14]J. Spector, H. L. Stormer, K. W. Baldwin, L. N. Pfeiffer, and K. W. West, Appl. Phys. Lett. **56**, 1290 (1990); **56**, 2433 (1990).
[15]T. Sakamoto, F. Nihey, and K. Nakamura, Appl. Phys. **63**, 3182 (1993).
[16]A. Kawabata, J. Phys. Soc. Jpn. **58**, 372 (1989).
[17]G. Kirczenow, Phys. Rev. B **39**, 10 452 (1989).
[18]A. Szafer and A. D. Stone, Phys. Rev. Lett. **62**, 300 (1989).
[19]Y. Avishai and Y. B. Band, Phys. Rev. B **40**, 3429 (1989).
[20]A. Weisshaar, J. Lary, S. M. Goodnick, and V. K. Tripathi, Appl. Phys. Lett. **55**, 2114 (1989); J. Appl. Phys. **70**, 355 (1991).
[21]T. Ando, Phys. Rev. B **44**, 8017 (1991).
[22]H. U. Baranger and A. D. Stone, Phys. Rev. Lett. **63**, 414 (1989).
[23]C. W. J. Beenakker and H. van Houten, Phys. Rev. Lett. **63**, 1857 (1989).
[24]M. L. Roukes and O. L. Alerhand, Phys. Rev. Lett. **65**, 1651 (1990).
[25]Y. Takagaki and D. K. Ferry, Phys. Rev. B **44**, 8399 (1991).
[26]R. A. Jalabert, H. U. Baranger, and A. D. Stone, Phys. Rev. Lett. **65**, 2442 (1990).
[27]H. Kasai, K. Mitsutake, and A. Okiji, J. Phys. Soc. Jpn. **60**, 1679 (1991); A. Okiji, H. Kasai, and A. Nakamura, Prog. Theor. Phys. Suppl. **106**, 209 (1991).
[28]R. Landauer, IBM J. Res. Dev. **1**, 223 (1957); **32**, 306 (1988).
[29]M. Büttiker, IBM J. Res. Dev. **32**, 317 (1988).
[30]M. Yosefin and M. Kaveh, Physica A **168**, 427 (1990).
[31]D. S. Fisher and P. A. Lee, Phys. Rev. B **23**, 6851 (1981).
[32]H. Tamura and T. Ando, Phys. Rev. B **44**, 1792 (1991).
[33]Y. Avishai and J. M. Luck, Phys. Rev. B **45**, 1074 (1992).
[34]S. E. Laux, D. J. Frank, and Frank Stern, Surf. Sci. **196**, 101 (1988).
[35]H. De Raedt, N. Garcia, and J. J. Saenz, Phys. Phys. Lett. **63**, 2260 (1989).
[36]M. Saito, M. Takatsu, M. Okada, and N. Yokoyama, Phys. Rev. B **46**, 13 220 (1992).
[37]A. Nakamura, Y. Maki, and A. Okiji, J. Phys. Soc. Jpn. **60**, 749 (1991); A. Okiji, H. Negishi, and A. Nakamura, *ibid.* **61**, 1145 (1992).
[38]K. Kawamura, T. Ueta, and H. Sawano, Jpn. J. Appl. Phys. **31**, 317 (1992); T. Ueta, J. Phys. Soc. Jpn. **61**, 4314 (1992).
[39]H. Yoshioka, and Y. Nagaoka, J. Phys. Soc. Jpn. **59**, 2884 (1990).
[40]T. Saku, Y. Hirayama, and Y. Horikoshi, Jpn. J. Appl. Phys. **30**, 902 (1991).

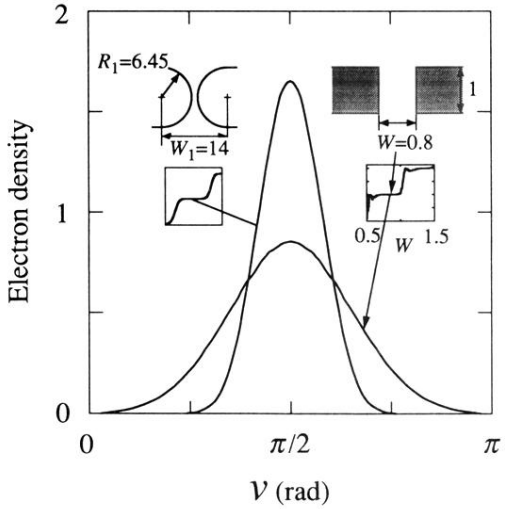

FIG. 5. Angular distribution of the injected electron at infinite distance from the point contact. A comparison of the collimation effect for a realistic and an abrupt configuration is given. Dimensions and conductance of the abrupt configuration are indicated in the inset. The electron density is normalized so that its angular integral is equal to the conductance (units of $2e^2/h$).

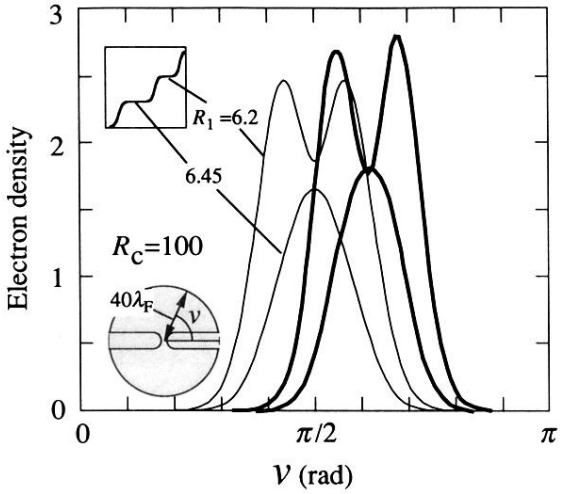

FIG. 6. Angular distribution under a magnetic field. Bold lines show the case for an applied magnetic field with $R_c = 100$ in a circle of radius 40. Narrow lines show the no-magnetic-field case. The distribution has a clearly single (double) peak structure in the case of $R_1 = 6.45(6.2)$, and the collimation also affects the propagation with the double peak.

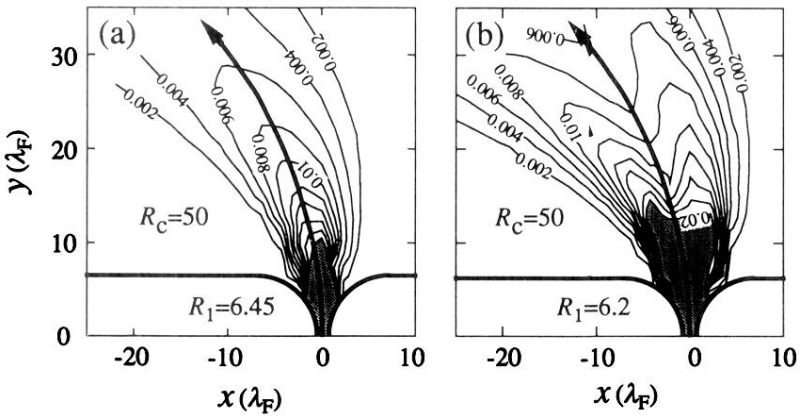

FIG. 7. Spatial distributions of the injected electrons under a magnetic field with $R_c = 50$. Bold arrows are classical cyclotron orbits. (a) $R_1 = 6.45$, (b) $R_1 = 6.2$. The shaded regions indicate an electron density greater than 0.02, since the contours would make the figure complex.

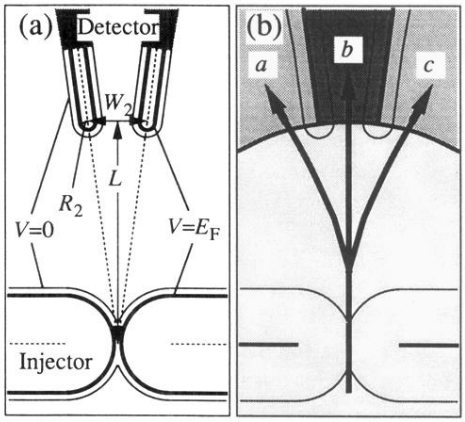

FIG. 8. Configuration of the device which consists of two point contacts as an injector and a detector. (a) Parameters of the detector are indicated. L is the distance between the detector's orifice and the injector. (b) Schematic picture illustrating the method of calculation of transfer conductance.

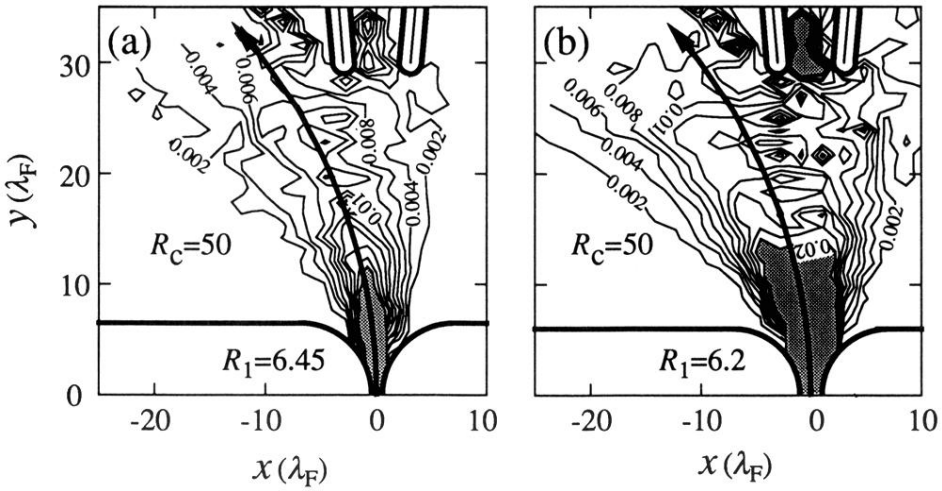

FIG. 9. Spatial distributions of the injected electron under a magnetic field with $R_c = 50$ with a wedge-shaped detector. (a) $R_1 = 6.45$, (b) $R_1 = 6.2$. The detector's parameters are $L = 30$, $R_2 = 1$, and $W_2 = 6$.